Appendix A. Supplementary Materials

1. Isotopic measurements

The aliquots for Os isotopic analysis were added into chilled Pyrex® Carius tubes, along with 5 ml of concentrated HNO_3 and 2.3 ml of concentrated HCl. The Carius tubes were sealed and then heated for at least 24 h at 220 °C (Shirey and Walker, 1995). Osmium was extracted from the solution using CCl_4 solvent-extraction methods (Cohen and Waters, 1996), and then further purified using microdistillation from a dichromate solution (Birck et al., 1997). This procedure resulted in ~70 % yield for Os. Between 70-300 ng of purified Os were loaded onto outgassed Pt filaments in HBr, activated with $Ba(OH)_2$, and analyzed as OsO_3^- by a *Thermo-Fisher Triton* thermal ionization mass spectrometer (TIMS) at the University of Maryland (UMd) (Walker, 2012). Osmium isotopic data were corrected for instrumental and natural mass fractionation by normalizing $^{192}Os/^{188}Os$ to 3.08271 (Allègre and Luck, 1980). Isobaric interferences from OsO_3^- species with ^{17}O or ^{18}O were corrected using the O isotopic composition reported by Nier (1950).

Molybdenum aliquots were prepared following the methods described in Worsham et al. (2016a). In brief, aliquots were dried, dissolved in 1 M HF, and loaded onto an anion column of AG 1-X8 (200-400 mesh) resin. Molybdenum was eluted using 6 M HNO_3-3 M HF, dried, and dissolved in 6 M HCl. The Mo solution was then added to a smaller anion column with ~0.3 mL AG 1-X8 (200-400 mesh) resin and eluted with 1 M HCl. This elution was repeated a second time. This procedure resulted in ~50 % yield for Mo. Purified Mo aliquots were treated with concentrated HCl and HNO_3 multiple times in order to destroy organics. The samples were then dissolved in 6 M HCl, about 500-1000 ng Mo were loaded onto outgassed Re filaments, and activated with ~ 2 µL of a 5 µg/µL $La(NO_3)_3$ solution. A double filament assembly was used and the same amount of $La(NO_3)_3$ was added to the ionization Re filament. Molybdenum was measured

as MoO_3^- by the *Thermo-Fisher Triton Plus* TIMS at UMd. The $^{100}Mo^{18}O^{16}O_2^-$ species was measured using a 10^{13} Ω resistor amplifier for O isotope interference corrections. Molybdenum isotopic data were corrected for instrumental and natural mass fractionation by normalizing $^{98}Mo/^{96}Mo$ to 1.453171 (Lu and Masuda, 1994).

Aliquots for Ru isotopic analysis were prepared following the procedure discussed by Bermingham et al. (2016). In brief, aliquots of the primary dissolution were dried and dissolved in 0.15 M HCl and then processed through a cation column of AG50WX8 (200-400 mesh) resin. Ruthenium was immediately eluted using 0.15 M HCl and dried to about 5 µL for microdistillation, in which $H_2Cr_2O_7$ was used as the oxidant and 6 M HCl was used as the trap solution and reductant. This procedure resulted in ~50 % yield for Ru. About 1000 ng of purified Ru were loaded onto outgassed single Pt filaments in HBr, activated with $Ba(OH)_2$, and analyzed as RuO_3^- by a *Thermo-Fisher Triton Plus* TIMS. Ruthenium isotopic data were corrected for instrumental and natural mass fractionation by normalizing $^{99}Ru/^{101}Ru$ to 0.745075 (Chen et al., 2010). The O isotopic composition reported by Nier (1950) was used to determine and correct for in-run ^{17}O and ^{18}O molecular interferences.

Tungsten aliquots from the primary dissolution were exposed to air for 1-2 weeks in order to oxidize Fe in the solution from +2 to +3. Ferrous Fe was then removed using a diisopropyl ether extraction procedure (Dodson et al., 1936). The resulting solution was dried, dissolved in 1 M HCl-0.1 M HF, and eluted through a cation column of AG50-X8 (200-400 mesh) resin with 1 M HCl-0.1 M HF. The solution was then dried, dissolved in 0.5 M HCl-0.5 M HF, loaded onto a column of AG1-X8 (100-200 mesh) resin, and eluted with 6 M HCl-1 M HF. This elution was repeated twice using progressively less resin and acid (Touboul and Walker, 2012). This procedure resulted in ~60 % yield for W. Organics accrued during the column chemistry were removed by

drying the sample multiple times in concentrated HCl and HNO_3. About 300-1000 ng of purified W were then dissolved in 1 M HCl- 0.01 M HF, loaded onto outgassed single Re filaments, activated with 1 µL of a 5 µg/µL La-5 µg/µL Gd solution, and measured as WO_3^- using a *Thermo-Fisher Triton* TIMS following the method of Archer et al. (2017). This method allowed independent measurement of both $^{182}W/^{184}W$ and $^{183}W/^{184}W$. Potential mass interference from ReO_3^- species were also monitored and corrected for. Tungsten isotopic data were corrected for instrumental and natural mass fractionation by normalizing $^{186}W/^{184}W$ to 0.92767 (Volkening et al., 1991).

Some prior studies of terrestrial and cosmochemical materials have observed deviations in $^{183}W/^{184}W$ ratios for reference standards and samples that were processed through certain column chemistry procedures and analyzed by multi-collector inductively-coupled plasma mass spectrometry (e.g., Kruijer et al., 2013; Cook and Schönbächler, 2016; Kruijer and Kleine, 2018). Such deviations have been interpreted to be the result of nuclear field shift effects, requiring corrections to be made to account for the observed deviations (Cook and Schönbächler, 2016). However, no such effects have been observed for reference standards, terrestrial samples, or meteorite samples using the column chemistry procedures described here, coupled with thermal ionization mass spectrometry (Archer et al., 2017; Mundl et al., 2017; Mundl et al., 2018; Archer et al., 2019). Consequently, no corrections to the measured $^{183}W/^{184}W$ ratios from this study have been made.

Values of $\mu^{182}W$ for the SBT were corrected for nucleosynthetic variations using the method reported by Kruijer et al. (2014a). In this correction, variation in the *r*-process component for irons is subtracted from the $\mu^{182}W$ value using $\mu^{183}W$ as an *r*-process component proxy. This correction is based on the $^{182/184}W$ *vs.* $^{183/184}W$ isotopic composition of fine- and coarse-grained CAI, which

give a $^{182/184}W$ *vs.* $^{183/184}W$ (186/184 normalized) correlation of +1.41 ± 0.06. The ΔT_{CAI} ages were then calculated using the CAI initial value $\mu^{182}W$ of -349 ± 7 (Kruijer et al., 2014b), the present-day chondritic $\mu^{182}W$ value of -190 ± 10 (Kleine et al., 2004), and the decay constant for ^{182}Hf of 0.078 ± 0.002 Myr^{-1} (Vockenhuber et al., 2004). The ΔT_{CAI} ages for Babb's Mill, South Byron, and ILD 83500 were calculated from the $\mu^{182}W$ and $\mu^{183}W$ values determined by normalizing to $^{186}W/^{184}W$. The uncertainties for the ΔT_{CAI} ages include the 2SD determined from the analysis of standards run during an analytical campaign for $\mu^{182}W$ and $\mu^{183}W$ compositions, and the uncertainty associated with the $\mu^{183}W$ *r*-process correction only (Kruijer et al., 2014a). Tungsten isotopic data were not obtained for Milton because there was insufficient material to make this measurement.

2. Fractional crystallization modeling

In this study, Eq. S1 is used to calculate the concentration of an element throughout the evolution of a liquid melt, where F_n is the fraction of liquid (n = 100 is pure liquid), C_{Ln} is the concentration of an element in the liquid phase at F_n, and D_n is the partition coefficient of an element. The concentration of an element is calculated at each 0.1 % fraction of liquid with respect to the concentration of the previous liquid fraction. For S, a constant partition coefficient of 0.001 is used (Walker et al., 2008). The partition coefficients for P and C are determined at each F_n by considering the concentration of S and P or S and C, respectively, in the liquid at F_{n+1}. Equation S2 is used to account for the effects of S on P and C partitioning behavior (Chabot and Jones, 2003).

Values of D_o for P and C are taken from Chabot et al. (2017) and Worsham et al. (2016b), respectively. The β_{SPC} variable is determined using Eq. S3 (Jones and Malvin, 1990), in which β_S

and β_P are taken from Chabot et al. (2017) and β_C is taken from Worsham et al. (2016b). For P, the effects of C are not considered and for C, the effects of P are not considered. The β_{SPC} and "Fe domains" (Eq. S4; Chabot et al., 2017) variables are calculated at each F_n, where X_i is the mole fraction of an element.

$$\text{Eq. S1: } C_{Ln-1} = \frac{C_{Ln}}{(F_{n-1} + 1 - F_{n-1}D_{n-1})}$$

$$\text{Eq. S2: } \frac{1}{D} = \frac{[\text{Fe domains}]^{\beta_{SPC}}}{D_o}$$

$$\text{Eq. S3: } \beta_{SPC} = \left[\frac{2X_S}{2X_S + 4X_P + 4X_C}\right]\beta_S + \left[\frac{4X_P}{2X_S + 4X_P + 4X_C}\right]\beta_P + \left[\frac{4X_C}{2X_S + 4X_P + 4X_C}\right]\beta_C$$

$$\text{Eq. S4: Fe domains} = \frac{1 - 2X_s - 4X_P - 4X_C}{1 - X_s - 3X_P - 3X_C}$$

$$\text{Eq. S5: } C_{Sn} = C_{Ln}D_n$$

After determining the concentration of S, P, and C at each F_n, the D values for the HSE are calculated at each F_n using Eq. S2-S4 by collectively considering the changes in S, P, and C content in the liquid (Jones and Malvin, 1990; Chabot and Jones, 2003; Worsham et al., 2016b; Chabot et al., 2017). The concentration of HSE in the liquid at each F_n is then determined using Eq. S1 and the solid composition (C_{Sn}) at each F_n is determined using Eq. S5.

3. Thermal accretion model

This study uses a thermal accretion model (Eq. S6) that describes a solid sphere, which gains heat through ^{26}Al decay and loses heat by conduction (Carslaw and Jaeger, 1959). The model solves for the temperature at a certain depth within the sphere at any time (t) after accretion and we assume that differentiation occurred instantaneously when the temperature halfway to the

center of the body from the surface reached 1600 K (Kruijer et al., 2017). This assumption is made since ~50 % of silicate melt fractions may be necessary for core formation (Taylor, 1992). In order to be consistent with past studies, we assume a radius of R = 40 km for the parent body and the temperature is evaluated at a depth of r = 20 km (Kruijer et al., 2017). The background nebular temperature is represented as T_0, thermal conductivity is represented as K, thermal diffusivity is represented as k, and a ^{26}Al decay constant of $\lambda = 9.83 \times 10^{-7}$ yr^{-1} is used with a Solar System initial ^{26}Al/^{27}Al ratio of 5.23×10^{-5} (Norris et al., 1983; Jacobsen et al., 2008). All values used in this model are listed in Table S1.

Eq. S6: $$T = T_o + \frac{kA}{K\lambda} e^{-\lambda t} \left(\frac{R \sin\left(r * \left(\frac{\lambda}{k}\right)^{\frac{1}{2}} \right)}{r \sin\left(R * \left(\frac{\lambda}{k}\right)^{\frac{1}{2}} \right)} - 1 \right) + \frac{2R^3 A}{r\pi^3 K} \sum_{n=1}^{\infty} \frac{(-1)^n}{n\left(n^2 - \frac{\lambda R^2}{k\pi^2}\right)} \sin\left(\frac{n\pi r}{R}\right) e^{-kn^2\pi^2 t/R^2}$$

The background temperature is assumed to be 250 K, consistent with models by Hevey and Sanders (2006), Kruijer et al. (2014b), and Kruijer et al. (2017), which is the average temperature estimated for a circumsolar disk at 2.5 AU and 1 Myr after T-Tauri star formation (Woolum and Cassen, 1999). The power per unit volume A (W m^{-3}) = H*ρ, where H is the power per unit mass (W kg^{-1}) and ρ is the density of the planetesimal (kg m^{-3}). The power per unit mass, H, is equal to (total Al atoms/kg)*(^{26}Al/^{27}Al)*(2.0 x 10^{-26} W/atom), where (^{26}Al/^{27}Al) is a function of time, the parent body concentration of Al is based off of the range observed in carbonaceous chondrites (0.86-1.68 wt. %; Lodders and Fegley, 1998), and the decay power of ^{26}Al is calculated from a decay energy of ^{26}Al of 6.4 x 10^{-13} J/atom with its half-life of 9.83 x 10^{-7} yr^{-1} (Hevey and Sanders, 2006). We note that this calculation of heat production differs from that reported by Kruijer et al. (2017). Kruijer et al. (2017) report using a range of Al concentration from 8.65-16.8 wt. %, which is an order of magnitude greater than used here. In addition, Kruijer et al. (2017) report calculating

heat production as A = Al concentration*($^{26}Al/^{27}Al$) and it is calculated in this study as A = (total Al atoms/kg)*($^{26}Al/^{27}Al$)*(2.0 x 10^{-26} W/atom)*(ρ), where ($^{26}Al/^{27}Al$) is a function of time in both models. Despite these differences between the model inputs, the results of both models differ by less than 0.2 Myr. For this study, 0.86 wt. % Al relates to A = 12.3*($^{26}Al/^{27}Al$), 1.20 wt. % Al relates to A = 17.1*($^{26}Al/^{27}Al$) and 1.68 wt. % Al relates to A = 23.9*($^{26}Al/^{27}Al$). Therefore, the results in this study for 0.86 wt. % Al and 1.20 wt. % Al are similar to the results by Kruijer et al. (2017) for 12 wt. % Al and 16.8 wt. % Al, respectively.

Supplementary Tables

Table S1

Osmium isotopic composition data for Milton and the SBT.

Sample	n[a]	$\mu^{189}Os$	2SD	$\mu^{190}Os$	2SD
Milton	1	-4	8	25	18
Babb's Mill	2	1	6	-4	7
Babb's Mill (*rep*)	1	8	7	-1	4
South Byron	3	8	7	-4	7
ILD 83500	1	3	6	-3	7

[a] n is the number of analyses. The reported $\mu^{189}Os$ and $\mu^{190}Os$ values reflect the average values obtained for each meteorite piece. Uncertainties reflect the largest (of n analyses) 2SD of the standards run during an analytical campaign.

Table S2

Terms and values used in the thermal accretion model.

Term	Symbol	Units	Value	Source
Al concentration	Al	Wt. %	0.86-1.68	Lodders and Fegley (1998)
Ambient temperature	T_o	K	250	Woolum and Cassen (1999)
Decay constant	λ	yr^{-1}	9.83×10^{-7}	Norris et al. (1983)
Decay energy	E	J $atom^{-1}$	6.4×10^{-13}	Hevey and Sanders (2006)
Density	ρ	kg m^{-3}	3200	Kruijer et al. (2017)
Diffusivity	k	m^2 s^{-1}	5×10^{-7}	Kruijer et al. (2017)
Initial $^{26}Al/^{27}Al$	$^{26}Al/^{27}Al_i$	atom/atom	5.23×10^{-5}	Jacobsen et al. (2008)
Power per unit mass	H	W kg^{-1}	[a]	
Power per unit volume	A	W m^{-3}	H x ρ	
Depth assessed for temperature	r	km	20	Kruijer et al. (2017)
Radius of body	R	km	40	Kruijer et al. (2017)
Thermal conductivity	K	W m^{-1} K^{-1}	2.1	LaTourrette and Wasserburg (1998)

[a] $H = (\text{Al atoms/kg})*(^{26}Al/^{27}Al)*(E*\lambda_{sec})$, where $(^{26}Al/^{27}Al)$ is a function of time and λ is in units of s^{-1}.

Supplementary Figures

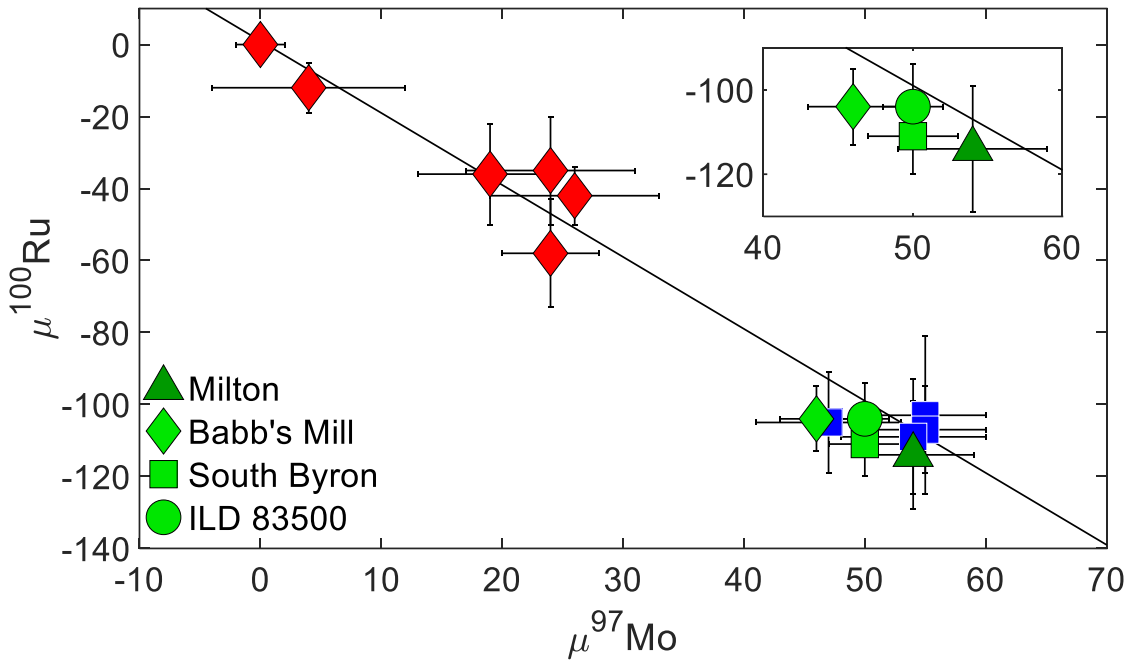

Fig. S1. Compilation of CRE-corrected μ^{97}Mo *vs*. μ^{100}Ru data for iron meteorites from Bermingham et al. (2018). Blue squares represent meteorites classified as CC type and red diamonds represent meteorites classified as NC type. Data from this study for the SBT and Milton are also plotted. The black line represents the regression of the Mo-Ru cosmic correlation from Bermingham et al. (2018). The inset shows the Mo and Ru isotopic composition of the SBT and Milton without other meteorites.

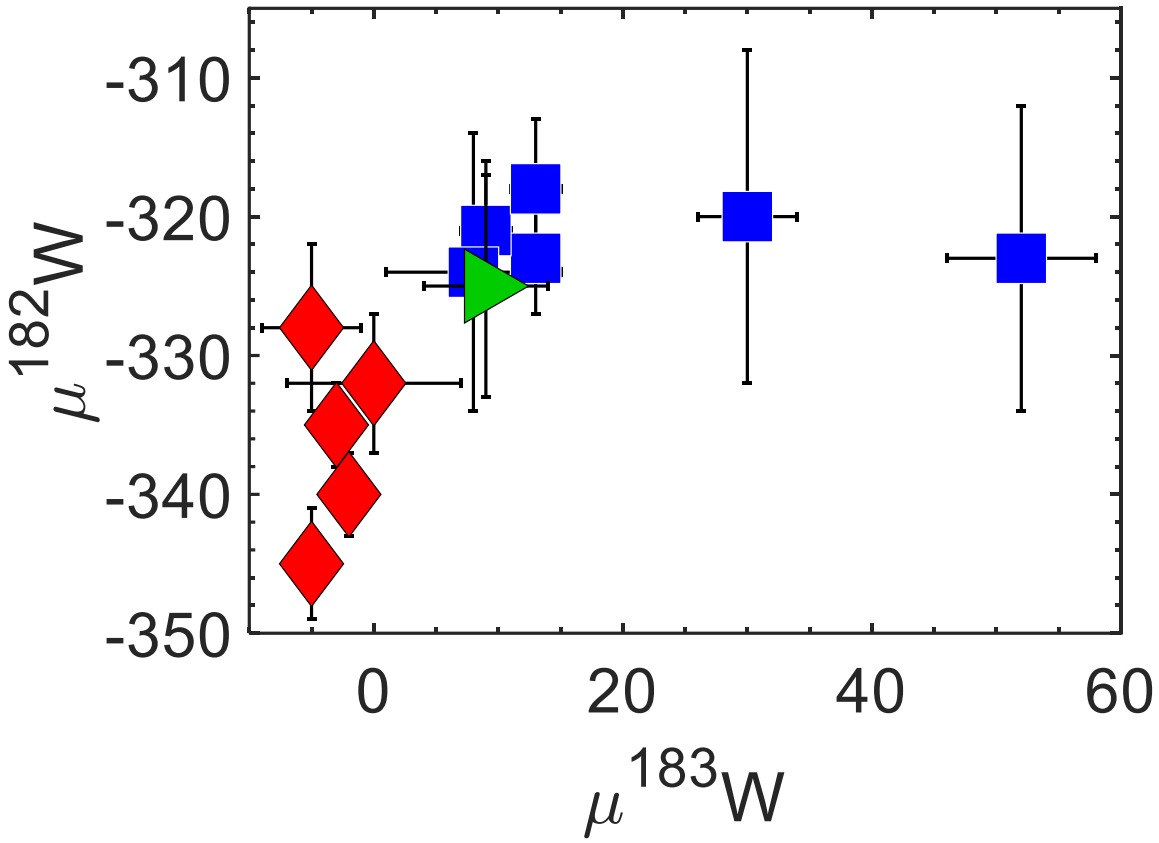

938

939 **Fig. S2**. Compilation of μ^{183}W *vs.* μ^{182}W data for iron meteorites from Kruijer et al. (2017). Blue
940 squares represent meteorites classified as CC type and red diamonds represent meteorites classified
941 as NC type. The average SBT W isotopic composition is also plotted (green triangle). The average
942 μ^{183}W value for the SBT (+9 ± 5, 2SE, n = 4) is resolved from the W standard value obtained
943 during the analytical campaigns for this work (0 ± 2, 2SE, n = 16).

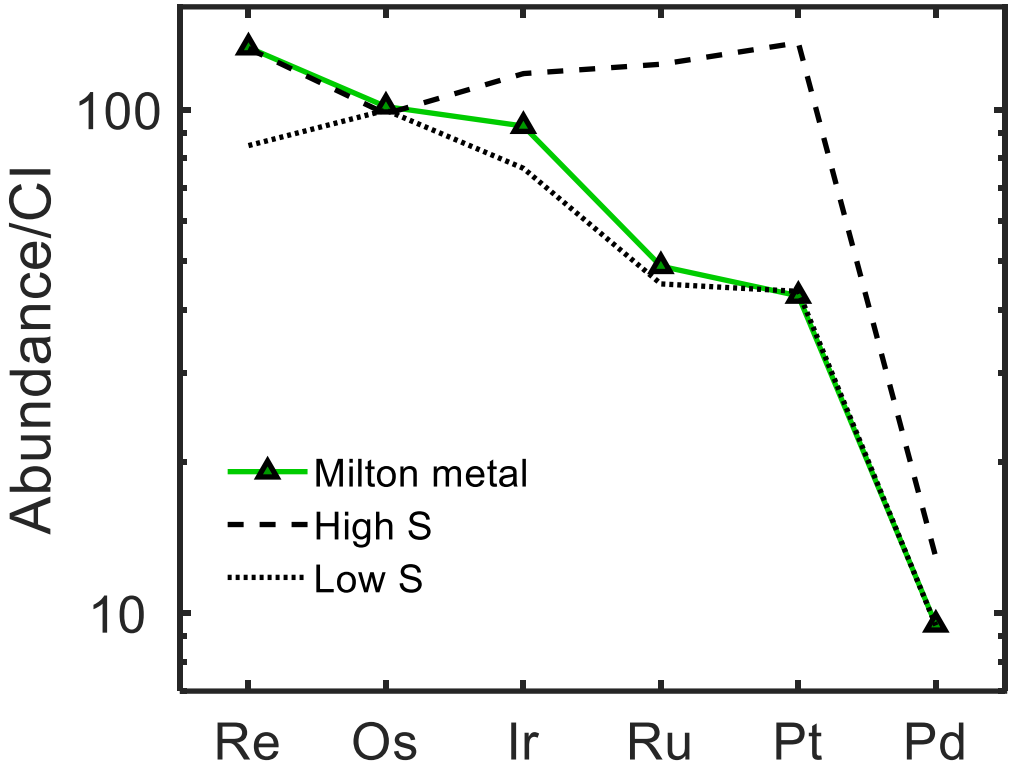

Fig. S3. CI-normalized HSE patterns calculated from a constant HSE initial concentration from Table 4 and varying S and P parental melt compositions. Assuming Milton metal crystallized in the first ~10% of solid, the Re/Os of Milton metal resembles a high S system with 17 wt. % S, 1.5 wt. % P, and <0.05 wt. % C. However, the Pt/Os of Milton metal resembles a lower S system with 8 wt. % S, 1 wt. % P, and <0.05 wt. % C.

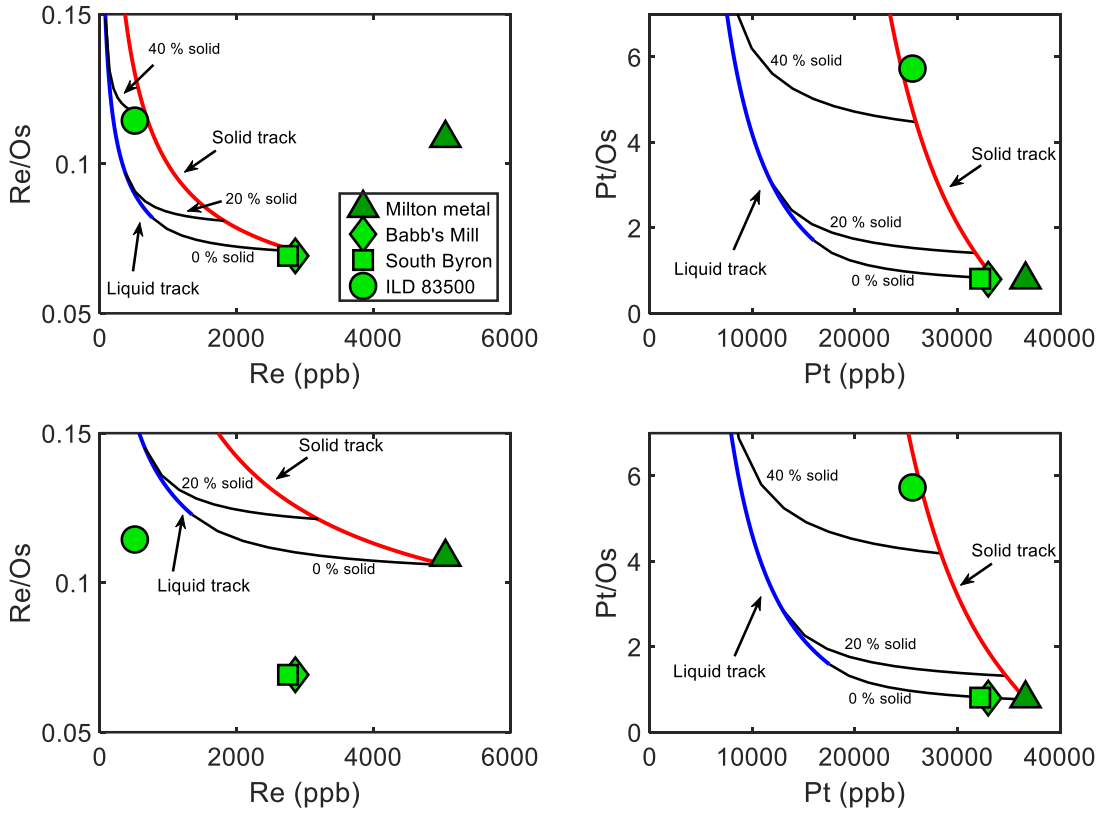

955

956 **Fig. S4**. Fractional crystallization models for Re (ppb) *vs*. Re/Os and Pt (ppb) *vs.* Pt/Os for two
957 pairs of parental melt compositions. Black lines represent mixing between solid and liquid, at 0 %
958 solid-100 % liquid, 20 % solid-80 % liquid, and 40 % solid-60 % liquid. (*Upper left and right*)
959 Fractional crystallization model, which reproduce the HSE patterns observed for the SBT,
960 calculated for the initial parameters listed in Table 4. (*Bottom left and right*) Fractional
961 crystallization model with 7 wt. % S and 1 wt. % P, which can reproduce the observed HSE
962 patterns for Milton metal. This model requires a starting liquid composition of Re = 1,350 ppb, Os
963 = 11,000 ppb, and Pt = 17,500 ppb. Neither model can reproduce both Re/Os and Pt/Os observed
964 in Milton metal and the SBT through solid metal-liquid metal mixing.

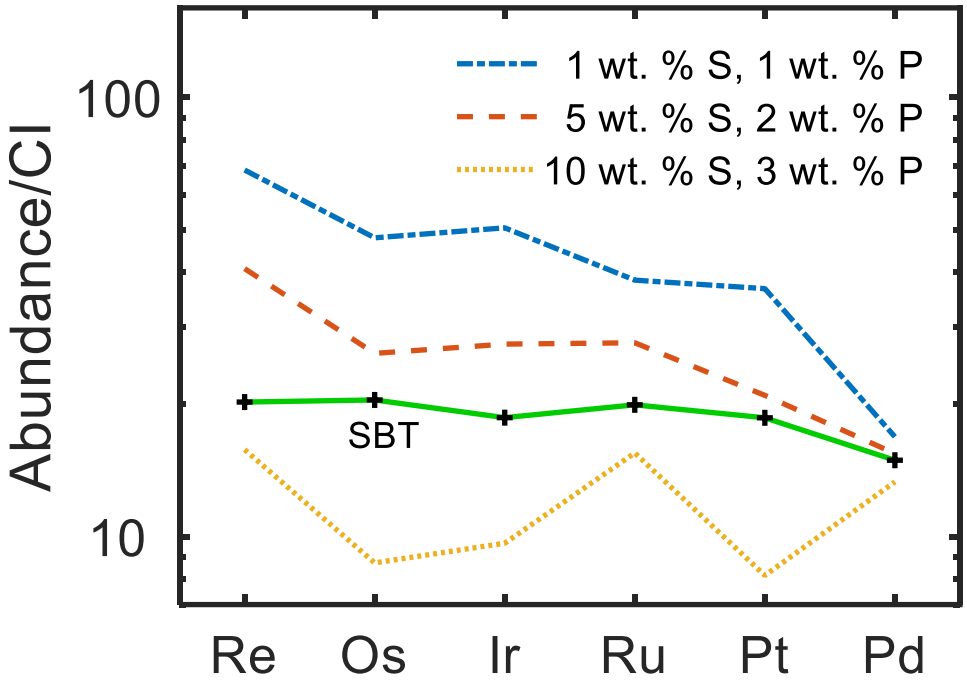

965

966 **Fig. S5**. CI-normalized HSE parental melt compositions, with varying S and P contents, which
967 reproduce the Milton HSE pattern as an early (<10 %) fractional crystallizing metal. The parental
968 melt composition of the SBT is shown for comparison.

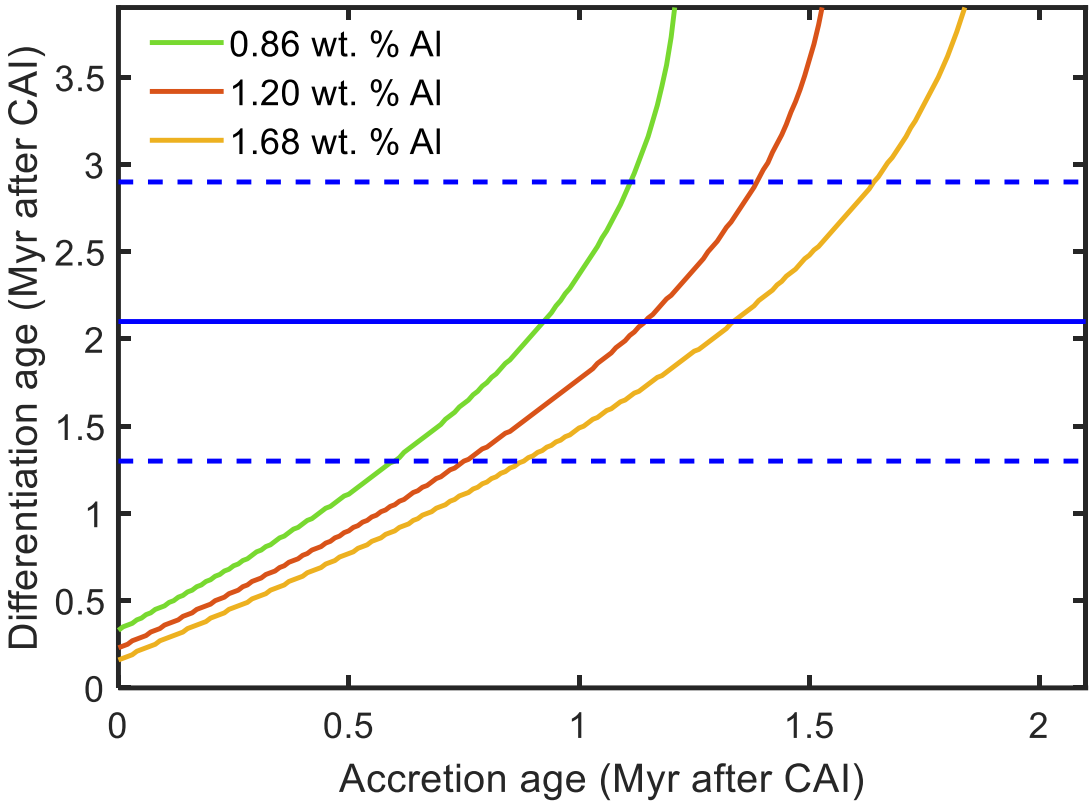

969

970 **Fig. S6**. Thermal model results for a 40 km radius body when evaluating the temperature midway
971 to the center of the body (r = 20 km). The model is based on an assumption of instantaneous
972 differentiation when the temperature reaches 1600 K. Thermal model results are shown for Al
973 concentrations of 0.86, 1.20, and 1.68 wt. %. The differentiation age of the SBT (2.1 ± 0.8 Myr
974 after CAI formation; blue solid line ± blue dashed lines) fits an accretion age range of 1.1 ± 0.5
975 Myr after CAI formation.

Supplementary References

Allègre C.J. and Luck J.-M. (1980) Osmium isotopes as petrogenetic and geological tracers. *Earth Planet. Sci. Lett.* **48**, 148–154.

Archer G.J., Mundl A., Walker R.J., Worsham E.A., Bermingham K.R. (2017) High-precision analysis of $^{182}W/^{184}W$ and $^{183}W/^{184}W$ by negative thermal ionization mass spectrometry: per-integration oxide corrections using measured $^{18}O/^{16}O$. *Int. J. Mass Spectrom.* **414**, 80-86.

Archer G.J., Walker R.J., Tino J., Blackburn T., Kruijer T.S., Hellmann J.L. (2019) Siderophile element constraints on the thermal history of the H chondrite parent body. *Geochim. Cosmochim. Acta* **245**, 556-576.

Bermingham K.R., Walker R.J., Worsham E.A. (2016) Refinement of high precision Ru isotope analysis using negative thermal ionization mass spectrometry. *Int. J. Mass Spectrom.* **403**, 15-26.

Bermingham K.R., Worsham E.A., Walker R.J. (2018) New insights into Mo and Ru isotope variation in the nebula and terrestrial planet accretionary genetics. *Earth Planet. Sci. Lett.* **487**, 221-229.

998 Birck J.-L., Roy-Barman M., Capmas F. (1997) Re–Os isotopic measurements at the femtomole
999 level in natural samples. *Geostand. Newsl.* **20**, 9–27.
1000
1001 Carlslaw H. S. and Jaeger J. C. (1959) *Conduction of heat in solids*. Oxford: Oxford University
1002 Press.
1003
1004 Chabot N. L. and Jones J. H. (2003) Parameterizing iron meteorite partitioning experiments.
1005 *Meteorit. Planet. Sci*. **37**, 1425–1436.
1006
1007 Chabot N.L., Wollack E.A., McDonough W.F., Ash R.D., Saslow S.A. (2017) Experimental
1008 determination of partitioning in the Fe-Ni system for applications to modeling meteoritic
1009 metals. *Meteorit. Planet. Sci* **52**, 1133-1145.
1010
1011 Chen J.H., Papanastassiou D.A., Wasserburg G.J. (2010) Ruthenium endemic isotope effects in
1012 chondrites and differentiated meteorites. *Geochim. Cosmochim. Acta* **74**, 3851–3862.
1013
1014 Cohen A.S. and Waters F.J. (1996) Separation of osmium from geological materials by solvent
1015 extraction for analysis by thermal ionization mass spectrometry. *Anal. Chimica Acta* **332**,
1016 269–275.
1017
1018 Cook D.L. and Schönbächler M. (2016) High-precision measurement of W isotopes in Fe-Ni alloy
1019 and the effects from the nuclear field shift. *J. Anal. At. Spectrom.* **31**, 1400-1405.
1020

Dodson R. W., Forney G. J., Swift E. H. (1936) The extraction of ferric chloride from hydrochloric acid solutions by isopropyl ether. *J. Am. Chem. Soc*. **58**, 2573-2577.

Hevey P.J. and Sanders I.S. (2006) A model for planetesimal meltdown by ^{26}Al and its implications for meteorite parent bodies. *Meteorit. Planet. Sci* **41**, 95-106.

Jacobsen B., Yin Q.-z., Moynier F., Amelin Y., Krot A.N., Nagashima K., Hutcheon I.D., Palme H. (2008) ^{26}Al-^{26}Mg and ^{207}Pb-^{206}Pb systematics of Allende CAIs: canonical solar system initial ^{26}Al/^{27}Al ratio reinstated. *Earth Planet. Sci. Lett.* **272**, 353-364.

Jones J. H. and Malvin D. J. (1990) A nonmetal interaction model for the segregation of the trace metals during solidification of Fe–Ni–S, Fe–Ni–P, Fe–Ni–S–P alloys. *Metall. Trans*. B 21B, 697–706.

Kleine, T., Mezger, K., Münker, C., Palme, H., Bischoff, A. (2004) ^{182}Hf–^{182}W isotope systematics of chondrites, eucrites, and Martian meteorites: chronology of core formation and mantle differentiation in Vesta and Mars. *Geochim. Cosmochim. Acta* **68**, 2935–2946.

Kruijer T.S., Fischer-Gödde M., Kleine T., Sprung P., Leya I., Wieler R. (2013) Neutron capture on Pt isotopes in iron meteorites and the Hf-W chronology of core formation in planetesimals. *Earth Planet. Sci. Lett*. **361**, 162-172.

Kruijer T.S., Kleine T., Fischer-Gödde M., Burkhardt C., Wieler R. (2014a) Nucleosynthetic W isotope anomalies and the Hf-W chronometry of Ca-Al-rich inclusions. *Earth Planet. Sci. Lett.* **403**, 317-327.

Kruijer T.S., Touboul M., Fischer-Gödde M., Bermingham K.R., Walker R.J., Kleine T. (2014b) Protracted core formation and rapid accretion of protoplanets. *Science* **344**, 1150–1154.

Kruijer T.S., Burkhardt C., Budde G., Kleine T. (2017) Age of Jupiter inferred from the distinct genetics and formation times of meteorites. *Proc. Natl. Acad. Sci.* **114**, 6712-6716.

Kruijer T.S. and Kleine T. (2018) No ^{182}W excess in the Ontong Java Plateau source. *Chem. Geol.* **485**, 24-31.

LaTourrette T. and Wasserburg G.J. (1998) Mg diffusion in anorthite: Implications for the formation of early solar system planetesimals. *Earth Planet. Sci. Lett*. **158**, 91–108.

Lodders K. and Fegley B. (1998) The Planetary Scientist's Companion. Oxford Univ Press, New York, 371 pp.

Lu Q. and Masuda A. (1994) The isotopic composition and atomic weight of molybdenum. *Int. J. Mass Spectrom. Ion Process*. **130**, 65–72.

Mundl A., Touboul M., Jackson M.G., Day J.M.D., Kurz M.D., Lekic V., Helz R.T., Walker R.J. (2017) Tungsten-182 heterogeneity in modern ocean island basalts. *Science* **356**, 66-69.

Mundl A., Walker R.J., Reimink J.R., Rudnick R.L., Gaschnig R.M. (2018) Tungsten-182 in the upper continental crust: Evidence from glacial diamictites. *Chem. Geol.* **494**, 144-152.

Nier A.O. (1950) A redetermination of the relative abundances of the isotopes of carbon, nitrogen, oxygen, argon, and potassium. *Phys. Rev.* **77,** 789–793.

Norris T.L., Gancarz A.J., Rokop D.J., Thomas K.W. (1983) Half-life of ^{26}Al. *J. Geophys. Res.* **88**, B331-B333.

Shirey S.B. and Walker R.J. (1995) Carius tube digestion for low-blank rhenium-osmium analysis. *Anal. Chem*. **34**, 2136-2141.

Taylor G.J. (1992) Core formation in asteroids. *J. Geophys. Res.* **97**, 14717-14726.

Touboul M. and Walker R.J. (2012) High precision tungsten isotope measurement by thermal ionization mass spectrometry. *Int. J. of Mass Spectrom.* **309**, 109-117.

Vockenhuber C., Oberli F., Bichler M., Ahmad I., Quittem G., Meier M., Halliday A.N., Lee D.-C., Kutschera W., Steier P., Gehrke R.J., Helmer R.G. (2004) New half-life measurement

of ^{182}Hf: Improved chronometer for the early solar system. *Physical Review Lette*rs **93**, 172501-1-172501-4.

Volkening J., Köppe M., Heumann K.G. (1991) Tungsten isotope ratio determinations by negative thermal ionization mass spectrometry. *Int. J. Mass Spectrom*. **107**, 361–368.

Walker R.J., McDonough W.F., Honesto J., Chabot N.L., McCoy T.J., Ash R.D., Bellucci J.J. (2008) Modeling fractional crystallization of group IVB iron meteorites. *Geochim. Cosmochim. Acta* **72**, 2198-2216.

Walker R.J. (2012) Evidence for homogeneous distribution of osmium in the protosolar nebula. *Earth Planet. Sci. Lett.* **351**-**352**, 36-44.

Woolum D. S. and Cassen P. (1999) Astronomical constraints on nebular temperatures: Implications for planetesimal formation. *Meteorit. Planet. Sci* **34**, 897–907.

Worsham E.A., Walker R.J., Bermingham K.R. (2016a) High-precision molybdenum isotope analysis by negative thermal ionization mass spectrometry. *Int. J. Mass Spectrom.* **407**, 51-61.

Worsham E.A., Bermingham K.R., Walker R.J. (2016b) Siderophile element systematics of IAB complex iron meteorites: new insights into the formation of an enigmatic group. *Geochim. Cosmochim*. *Acta* **188**, 261-283.